Supporting Information

Making Room for Reactivity in Topochemical Transformations under Pressure

Tengteng Lyu, Jonathan B. Lefton, Martin Etter, Shrikant Bhat, Wenhao Liu, Bing Lv, Luke J. Kwan, Hao Yan, Tomče Runčevski

Materials synthesis

Solvothermal synthesis of Co(OH)(sorb). Deionized water (400 mL) was sparged for 1 h prior to the addition of cobalt(II) nitrate hexahydrate (11.6 g, 40 mmol) and potassium sorbate (12.0 g, 80mmol). The sparge was removed, a pressure cap applied, and the bottle was transferred to a 90 °C oven for 16 h. The supernatant containing the pink solid was decanted, and the solid was soaked in deionized water at 90 °C for 24 h. After one additional round of decant/soaking, the pink solid was collected by vacuum filtration and dried on the bench for 24 h. The crystal structure[1] is described in the *P*21/*c* space group with unit cell parameters of a = 6.5584(6) Å, b = 6.3255(5) Å, c = 16.837(1) Å, β = 89.70(1)° and V = 698.5(1), measured at 100 K.

Solvothermal synthesis of Mn(sorb)$_2$. Manganese(II) nitrate tetrahydrate (7.2 g, 40 mmol) was prepared in the same way as above, resulting in a yellow, crystalline solid.

Multi-anvil high pressure synthesis

The room-temperature high pressure experiment was performed using a six-ram Hall-type large volume press (mavo press LPQ6 1500-100; Max Voggenreiter GmbH, Germany) 'Aster-15' at beamline P61B at DESY, Hamburg.[2] Tungsten carbide second stage anvils (32 mm Fujilloy TF08) with a truncated edge length of 4 mm were used to compress a 10 mm MgO octahedron (Cr_2O_3 doped) pressure transmitting medium. The orange-colored powder sample was placed inside the MgO capsule (ID 2.0 mm and h =2.0 mm) in the centre of the octahedron (see Figure S6a). All high-pressure parts were fired at 1000°C for 2h and kept at 100°C over night before compression. The target pressure of approximately 20 GPa was reached in 4h of compression time, followed by a 2h hold time and finally an overnight decompression (12h). The pressure (oil pressure in bar) applied to the sample is calculated based on the pressure calibration for the particular assembly and configuration.
After the experiment, the MgO octahedron was broken and the octahedron and the MgO capsule were removed from the sample. The sample itself exhibits a visible change to purple color (see Figure S6b).

Hydrostaticity of the silicone oil PTM

We use the splitting of ruby's R1 and R2 fluorescence peaks, as well as the change of R1's width, to gauge the hydrostaticity of the silicone oil PTM in the pressure range encountered in this work. The R1-R2 splitting fluctuates about 29 cm^{-1} from 2 to 14 GPa, and increases to 34 cm^{-1} at 16 GPa. The change of R1 width varies between 0 and 5.5 cm^{-1} from 2 to 16 GPa. These values are comparable to literature and consistent with a quasi-hydrostatic pressure.[3] We note that the slight deviation from hydrostaticity may actually encourage the anisotropic deformation that leads to reaction.

In situ high pressure techniques

High-pressure *in situ* characterizations are carried out in a symmetric diamond anvil cell (SymmDAC, Almax Easylab) fitted with type IIas ultralow fluorescent background diamond anvils. Pre-indented and micro-drilled stainless steel gaskets are used to define the sample chamber. Dry silicone oil (dynamic viscosity = 5 cSt at 25 °C, Sigma Aldrich) is used as the pressure transmitting medium (PTM) unless otherwise specified. Pressure is calibrated with the fluorescence of a ruby microsphere[4] loaded together with the sample. Pressure is changed quasi-statically with 2-3 GPa steps.

In situ Raman spectroscopy

High-pressure Raman spectra are collected on a Renishaw InVia confocal micro-spectrometer fitted with 1800 l/mm grating and a CCD detector, affording a spectral resolution of ~1 cm^{-1}. All measurements are performed using a 100-mW, 785-nm excitation laser attenuated to 50% power with a neutral-density (ND) filter. The laser is focused on the sample plane with a 50x objective resulting in a ~1 μm^2 spot size. Each spectrum is collected with 1-s exposure and 128 integrations. We note that samples in the DAC tend to become thinner upon compression and do not usually recover upon release of pressure. Additionally, pressure may dampen some of the vibrational modes. These factors account for the reduced Raman intensity and signal-to-noise ratio in some high-pressure and recovered samples.

In situ ultraviolet-Visible (UV-Vis) Absorption Spectroscopy

The transmission-mode UV-vis spectra are collected by a home-built UV-vis microspectrophotometer that utilize white-light emission (190 – 2500 nm) from a deuterium-halogen lamp (SL4-DH, StellarNet) and a 20x finite-corrected reflective objective lens (Edmund Optics). The details of our home-built UV-vis microspectrophotometer are published in previous paper.[5] A thin layer of powder sample is loaded with ruby ball in the DAC, and the DAC is amounted in a custom cell holder on the XYZ stage. The dark spectrum is collected with no light entering the spectrometer. The reference spectrum is collected from an area with no sample (large circles on the left side of the samples, Fig. 2d). Pressure is calibrated with ruby microspheres (small circles on the right side, Fig. 2d). The absorbance (Abs) is calculated as:

$$Abs = \ln \frac{I_{ref} - I_{dark}}{I_s - I_{dark}}$$

where I_{ref}, I_{dark} and I_s are the light intensities from the reference, dark background, and sample, respectively. The UV-Vis spectra of the pristine sample and decompressed sample are collected.

In situ powder X-ray powder diffraction (PXRD)

In situ PXRD are measured at beamline 12.2.2, Advanced Light Source, Lawrence Berkeley National Laboratory. Dry powder samples are mixed with MgO (10 wt%) and loaded in the DAC without liquid PTM. X-ray energy is 25 keV (wavelength: 0.496 Å) and typical spot size is 5 mm × 5 mm. Diffraction patterns are collected in the transmission (Debye-Sherrer) geometry using a MAR345 detector. LaB_6 powder is used for calibration. Pressure is calibrated using the (220) diffraction peak of MgO. Debye ring integration is performed with Dioptas.[6]

Density-Functional Theory

High-pressure crystal structures are simulated using the Perdew–Burke-Ernzerhof (PBE) level of DFT with plane-wave basis sets and the standard solid-state pseudopotential (SSSP) set,[7] implemented in Quantum ESPRESSO.[7] The energy cutoffs for the wave function and charge density are set at 60 and 600 Rydberg (Ry), respectively. Geometry optimizations are performed under hydrostatic pressures from 0 to 65 GPa. Convergence thresholds are 10^{-6} Ry for SCF iteration, 10^{-4} Ry for total energy, 10^{-3} Ry per Bohr radius for force, and 0.1 GPa for pressure. Subsequently, the structure at 65 GPa is quenched back to 0 GPa in steps of 5 GPa.

Raman and ^{1}H-NMR spectra of sorbic acid monomers and oligomers are simulated at the B3LYP/6-311G(d,p) level of DFT implemented in Gaussian. A universal scaling factor of 0.964 is applied to the calculated frequencies.[8] Dispersion correction is incorporated using Grimme's D3 scheme with Becke-Johnson damping. The NMR of tetramethylsilane (TMS) is simulated at the same level of theory as reference. These simulations yield the isotropic shielding (σ) from which the chemical shift is calculated as $\delta(ppm) = (\sigma_{TMS} - \sigma_{sorbate}) \times 10^6$

We emphasize that the purpose of the calculated Raman is not to reproduce the line shape of the experimental data, but rather to show that the number of non-degenerate C=C stretching modes increases with polymerization, therefore providing an interpretation of the observed line broadening (Fig. 2a) and supporting the proposed mechanism.

Deviation between experimental and DFT-computed transition pressure

The computed transition pressure in Co(OH)(sorb), 35 GPa, is significantly higher than the experimentally observed value, ~10 GPa. We note that polymerization in the DFT simulation is achieved by a series of relaxations of the crystal structure at incremental pressures. Several factors may contribute to the deviation:

1. The relaxation is performed using the Broyden–Fletcher–Goldfarb–Shanno (BFGS) local optimization algorithm; as such, it can only find minimal-energy structures in the vicinity of the input structure, without any barriers separating the two on the potential energy surface. In experiments, the activation barrier can be overcome by thermal excitation.
2. Our modeling has assumed that pressure is uniform across the crystal, and reaction of the sorbates commences simultaneously in each unit cell. In reality, local initiation of the reaction may occur through variations of the local stress and strain, lowering the onset pressure of polymerization.

Crystal structure solution of Mn(sorb)$_2$

The powder X-ray diffraction pattern of Mn(sorb)$_2$ (Figure S10) was collected on a high-resolution laboratory Stoe Stadi-P powder diffractometer, operating in Debye−Scherrer (transmission) geometry. The diffractometer was equipped with a molybdenum X-ray source. Monochromatic Mo-*K*α$_1$ radiation was obtained by a primary Ge(111) monochromator (centered at 0.7093 Å). Scattered X-ray intensity was simultaneously collected by two highly sensitive, linearly positioned silicon-strip (Mythen Dectris 1K) detectors. Sample preparation involved very gentle grinding of the materials in a pestle and packing in borosilicate capillaries with a 0.5 mm diameter. During measurements, the capillary was rotated for improved particle statistics. Diffraction data was collected at room temperature for 24h.
The powder X-ray diffraction pattern was analyzed using the TOPAS-Academic V6 software (Coelho Software, 2018). Initial indexing was carried out through the singular value decomposition function,[9] which suggested a monoclinic unit cell and pointed toward a likely *P*2$_1$/*c* space group symmetry, later confirmed through Rietveld refinement.[10] Accurate unit cell parameters were obtained via structureless Pawley fitting,[11] implemented with the fundamental parameter approach.[12] During this procedure, unit cell dimensions, background coefficients (modeled using a Chebyshev polynomial), and peak shape/instrumental contributions (based on the simple axial divergence model) were refined concurrently.
With the Pawley fit completed, structure solution proceeded using the refined cell parameters and the *P*2$_1$/*c* space group. This was achieved by a real-space global optimization approach employing simulated annealing with the Metropolis algorithm.[13] To limit the number of variables, the sorbate fragment was defined as a rigid body using Z-matrix notation.[14] Given the asymmetric unit volume, one sorbate and one Mn were included in the model.
Throughout the simulated annealing process, bond lengths and angles within the rigid body were held constant, while dihedral angles were permitted to vary. The rigid units were translated and rotated freely within the asymmetric unit until the algorithm converged on a global minimum. Following convergence, the resulting model underwent whole-pattern Rietveld refinement.[10] Hydrogen atoms were added geometrically. During this final refinement step, all previous parameters were refined again—alongside unit cell dimensions, peak shape parameters, background function, internal geometry of the rigid bodies (under soft restraints), and thermal displacement parameters (defined as a single value per atomic species, excluding hydrogens, which were assigned 1.5× the displacement of their bonded atom).

The Rietveld refinement produced satisfactory convergence with reliable agreement factors and a clean difference plot. The final Rietveld profile and key refinement parameters are given in Table S1, and the data is presented in Figure S10.

Table S1. Crystallographic and refinement details for $Mn(sorb)_2$

λ (Å)	0.7093
T (K)	293
2θ range (°)	1.75 - 25
Time (h)	20
molecular formula	$Mn(C_6H_7O_2)_2$
crystal system	Monoclinic
space group	$P2_1/c$
a (Å)	20.292(3)
b (Å)	4.9241(4)
c (Å)	6.1275(4)
α (°)	90
β (°)	110.950(9)
γ (°)	90
V (Å)	571.7(1)
R_{exp} (%)	0.05
R_p (%)	7.28
R_{wp} (%)	8.94
R_{bragg} (%)	2.58
No. of variables	40

Table S2. DFT-computed lattice parameters of $Mn(sorb)_2$.

Pressure (GPa)	a (Å)	b (Å)	c (Å)	α (°)	β (°)	γ (°)	Unit cell volume (Å^3)
-0.06	20.201	4.652	5.673	90	111.085	90	497.423
10.016	18.179	4.484	5.268	90	104.939	90	414.908
14.965	17.575	4.434	5.182	90	102.94	90	393.554
19.965	17.191	4.382	5.114	90	101.735	90	377.191
25.016	16.844	4.344	5.055	90	100.615	90	363.602
29.948	16.672	4.302	4.996	90	99.968	90	352.874
35.012	16.181	4.29	4.983	90	98.697	90	341.984
40.016	15.992	4.261	4.942	90	98.077	90	333.415
44.981	15.574	4.267	4.929	90	97.023	90	325.092
50.015	15.418	4.237	4.901	90	96.573	90	318.053
54.971	15.128	4.233	4.887	90	95.813	90	311.394
60.036	14.962	4.209	4.872	90	95.416	90	305.405
65.009	14.859	4.188	4.843	90	95.08	90	300.17
59.998	14.947	4.211	4.874	90	95.383	90	305.403
54.975	15.076	4.236	4.898	90	95.766	90	311.221
50.038	15.261	4.254	4.922	90	96.263	90	317.643
45.047	15.498	4.27	4.944	90	96.877	90	324.804
39.944	15.819	4.279	4.966	90	97.769	90	333.019
34.98	16.03	4.311	4.997	90	98.325	90	341.623
30.002	16.387	4.322	5.035	90	99.37	90	351.81
24.989	16.798	4.341	5.072	90	100.559	90	363.59
19.996	17.049	4.392	5.131	90	101.367	90	376.646
14.985	17.525	4.426	5.203	90	102.877	90	393.443
9.979	18.103	4.473	5.297	90	104.766	90	414.738
4.984	18.89	4.535	5.435	90	107.372	90	444.418
-0.038	20.416	4.645	5.655	90	111.638	90	498.466

Table S3. DFT-computed lattice parameters of Co(OH)(sorb).

Pressure (GPa)	a (Å)	b (Å)	c (Å)	α (°)	β (°)	γ (°)	Unit cell volume (Å^3)
-0.024	5.164	6.843	19.259	90	81.103	90	672.37
4.966	5.067	6.697	17.466	90	71.393	90	561.609
9.942	4.942	6.62	17.021	90	68.787	90	519.132
14.914	4.866	6.526	16.746	90	67.29	90	490.548
19.817	4.788	6.471	16.541	90	66.27	90	469.131
24.803	4.713	6.451	16.377	90	65.012	90	451.27
29.949	4.651	6.41	16.236	90	64.178	90	435.647
35.009	4.546	6.468	15.819	90	61.382	90	408.353
39.975	4.521	6.396	15.73	90	61.129	90	398.263
30.034	4.576	6.559	15.905	90	61.534	90	419.609
25.026	4.606	6.66	16.008	90	61.735	90	432.477
20.03	4.638	6.773	16.123	90	61.998	90	447.16
14.957	4.685	6.889	16.246	90	62.253	90	464.089
9.947	4.726	7.039	16.412	90	62.805	90	485.692
5.034	4.781	7.222	16.616	90	63.464	90	513.296
-0.019	4.843	7.497	17.122	90	64.795	90	562.512

Table S4. XRD-determined interlayer d_{001} of Co(OH)(sorb).

Pressure (GPa)	d_{001} (Å)
0.0	17.05
2.5	15.89
5.5	15.44
7.0	15.35
10.5	15.24
13.5	15.35
9.5	15.49
6.5	15.66
4.0	15.92
2.5	16.07
0.5	16.40

Table S5. XRD-determined interlayer d_{100} of $Mn(sorb)_2$.

Pressure (GPa)	d_{100} (Å)
0.0	18.91
2.3	18.42
4.1	18.07
5.1	17.73
5.5	17.62
9.3	17.51
13.5	17.40
15.9	17.40
12.1	17.40
11.7	17.51
6.5	17.62
2.7	18.07
0.9	18.07

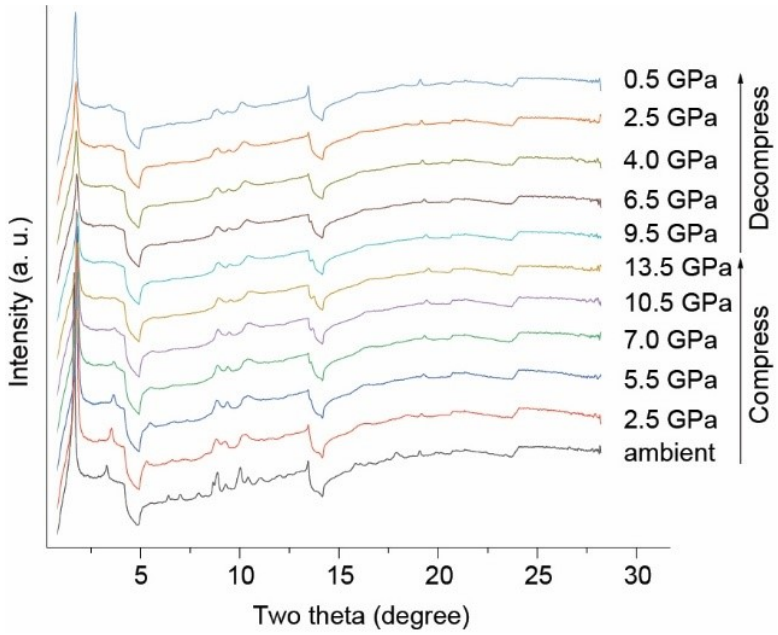

Figure S1. High-pressure powder X-ray diffraction (PXRD) patterns of Co(OH)(sorb). (Wavelength of 0.496 Å).

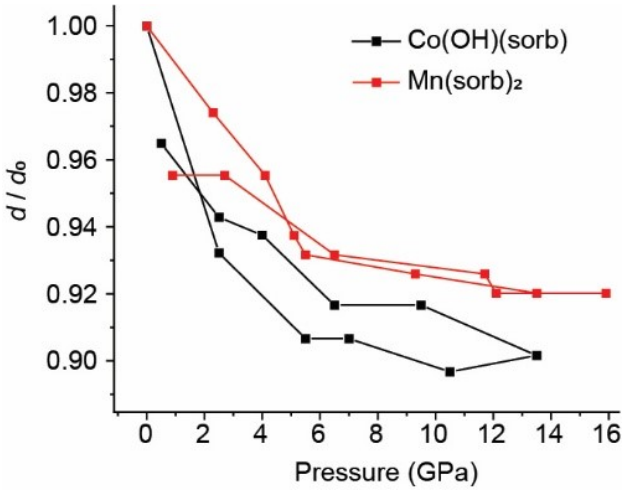

Figure S2. XRPD-derived Interlayer spacing normalized by that at ambient pressure.

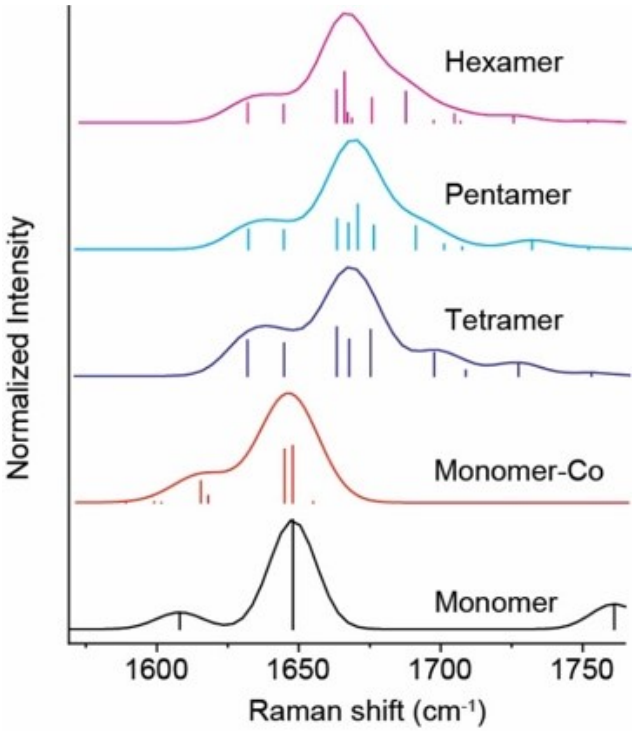

Figure S3. DFT-computed Raman spectra of mono- and oligo-meric sorbic acid, as well as monomeric cobalt(II) sorbate. Vertical lines indicate the frequencies of the normal modes. An arbitrary Gaussian broadening of 25 cm^{-1} is added to generate the simulated spectra.

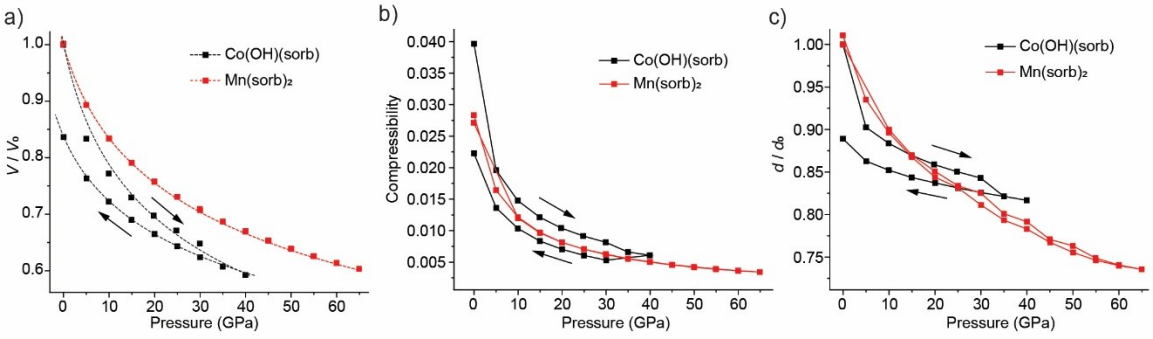

Figure S4. DFT-computed compressibility. (a) Unit cell volume normalized by that at ambient pressure. The dashed lines denote fitting to the third-order Birch-Murnaghan equation of state. For Co(OH)(sorb), fitting is performed separately for the compression and decompression data; for $Mn(sorb)_2$, a single fitting is performed on both compression and decompression data. (b) Volumetric compressibility ($-\frac{1}{V}\frac{dV}{dp}$) versus pressure. (c) Interlayer distance normalized by that at ambient pressure. The arrows in (a-c) denote the direction of pressure ramping for Co(OH)(sorb).

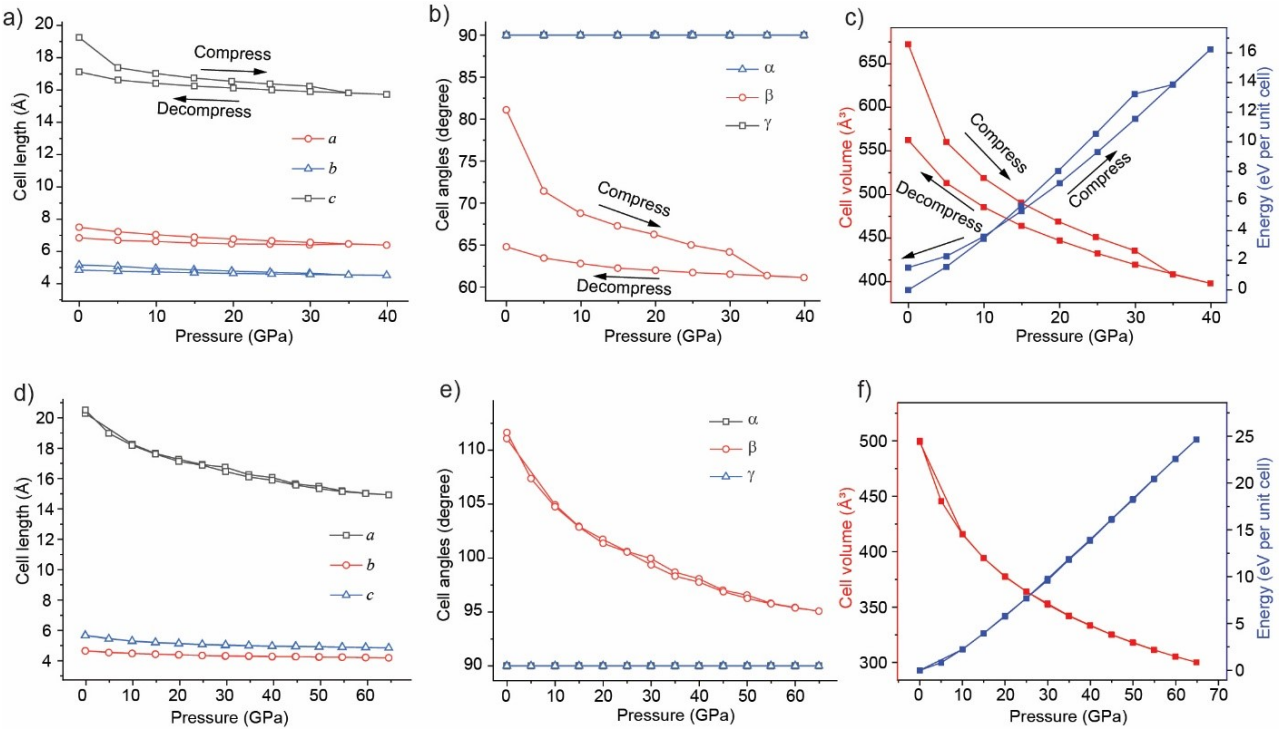

Figure S5. Direct comparison of the DFT-computed cell parameters and total energies changes of (a-c) Co(OH)(sorb) and (d-f) $Mn(sorb)_2$ upon compression and decompression.

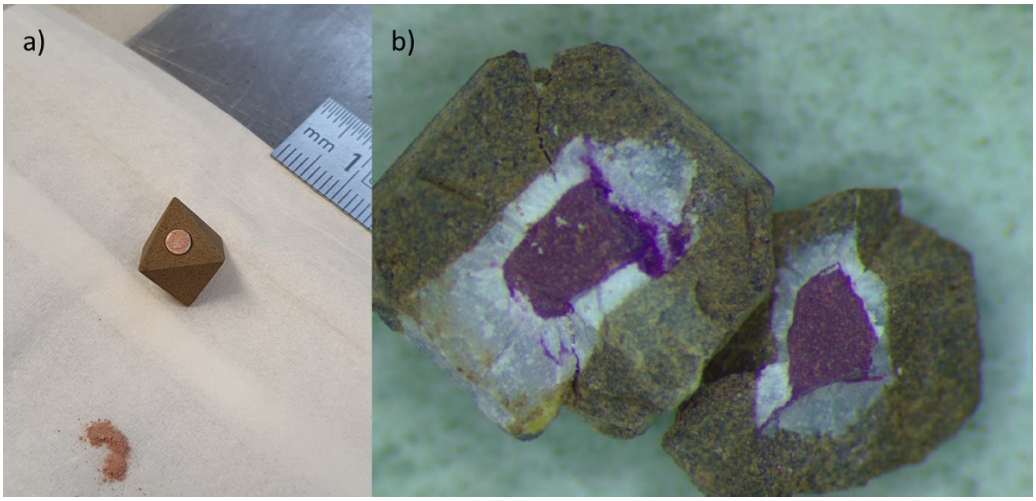

Figure S6. Orange colored powder sample placed in a MgO capsule which is inserted in a MgO octahedron (Cr_2O_3 doped). b) Broken MgO octahedron and MgO capsule after the experiment. The color of the sample has changed from orange to purple.

Figure S7. Photograph of the remaining material after dissolving HP-Co(OH)(sorb), swelling in the NMR solvent [DCl/D_2O/CD_3OD (25 µL 35% DCl in D_2O, 500 µL CD_3OD)] after the cobalt^{2+} cations, and OH^- and unreacted sorb$^-$ anions have leached out.

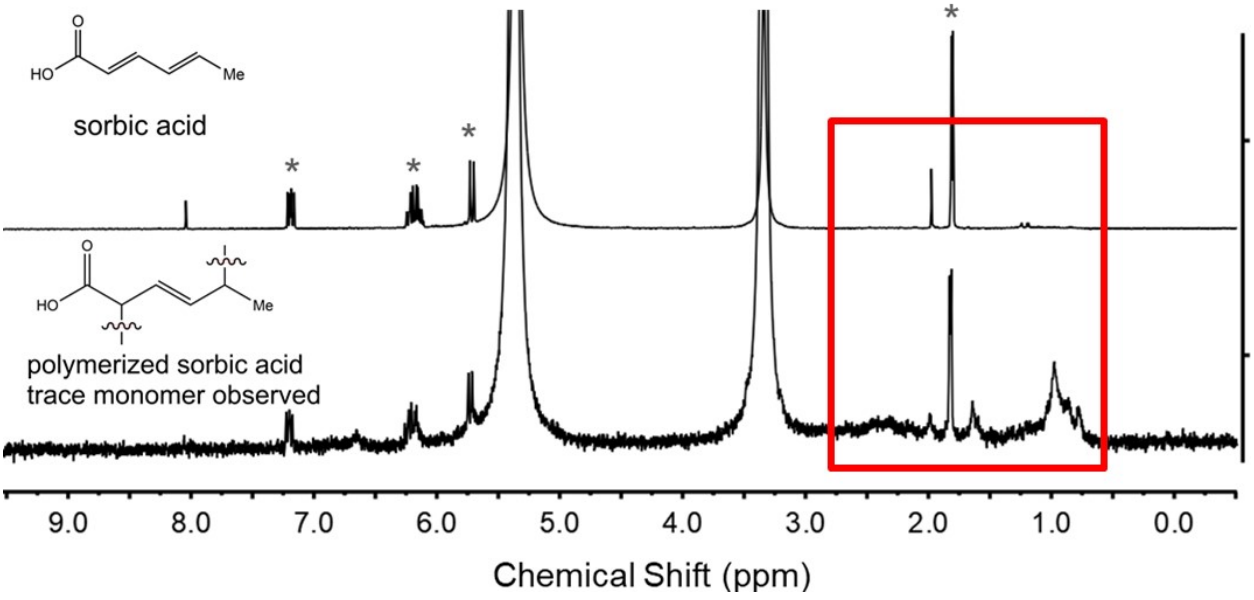

Figure S8. ^{1}H NMR spectra overlay, showing the non-pressed sample (top) and pressed sample (bottom). The spectra are shown on relative scale, normalized to the sorbic acid peaks, to highlight the differences in the pressed sample. The pressed sample, in addition to lower overall intensity, contains two notable broad peaks (highlighted by the red box) centered at 0.97 ppm and 1.67 ppm. Sorbic acid peaks are labelled with asterixis. Both samples were digested in a DCl/D_2O/CD_3OD (25 µL 35% DCl in D_2O, 500 µL CD_3OD) solvent and the ^{1}H NMR spectra were obtained on a JEOL 500 MHz spectrometer.

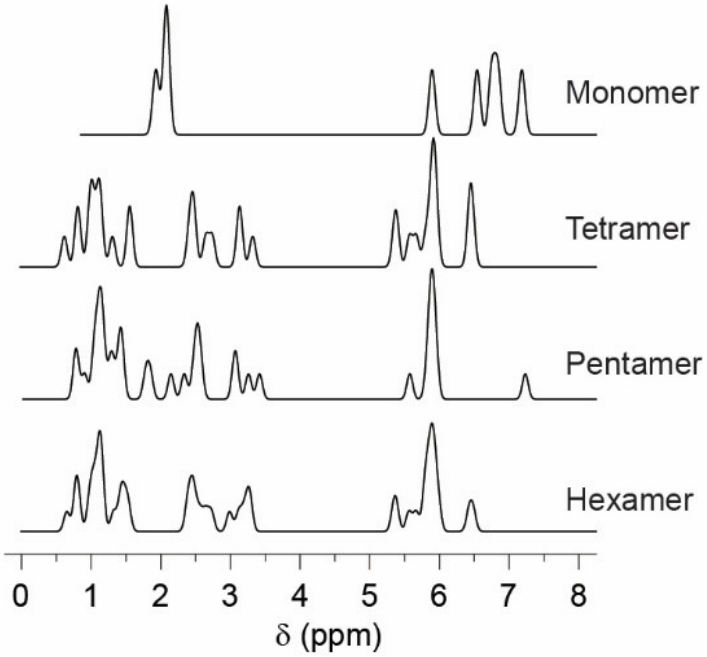

Figure S9. DFT-computed ^{1}H-NMR of mono- and oligomeric sorbates.

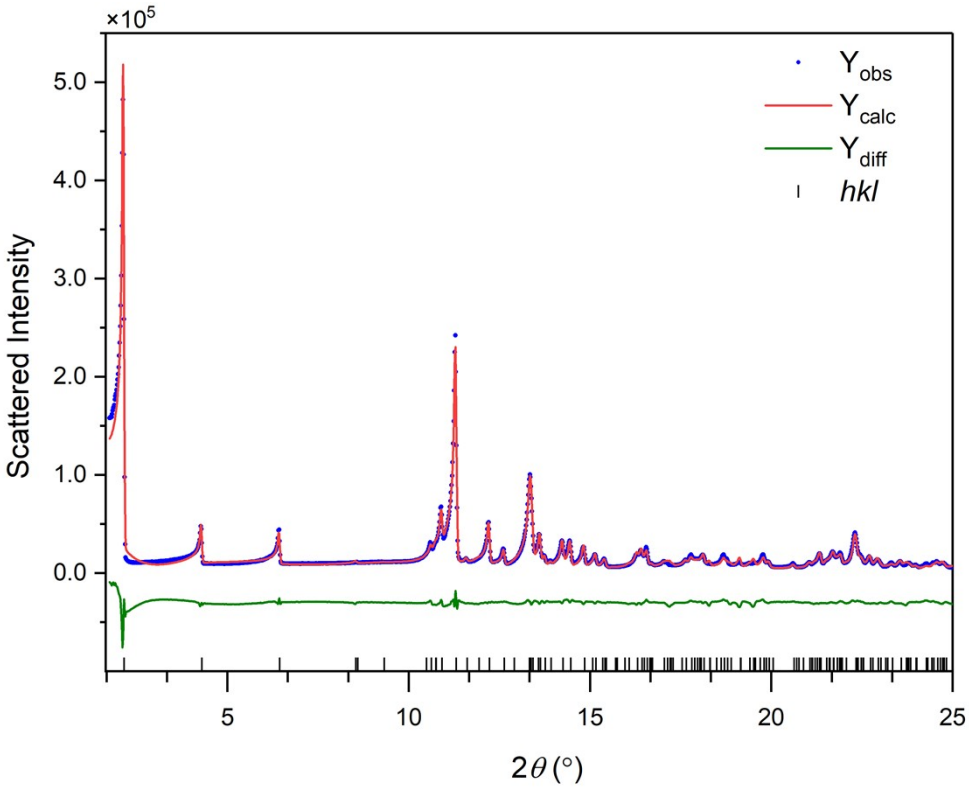

Figure S10. Rietveld refinement of $Mn(sorb)_2$ against the powder X-ray diffraction pattern. (Wavelength of 0.7093 Å).

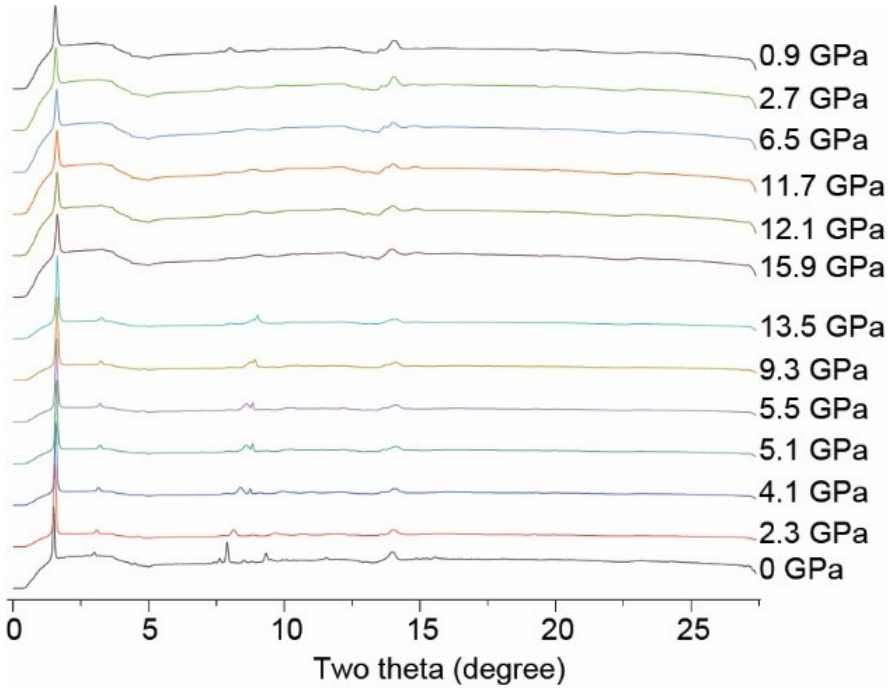

Figure S11. High-pressure powder X-ray diffraction (PXRD) patterns of $Mn(sorb)_2$. (Wavelength of 0.496 Å).

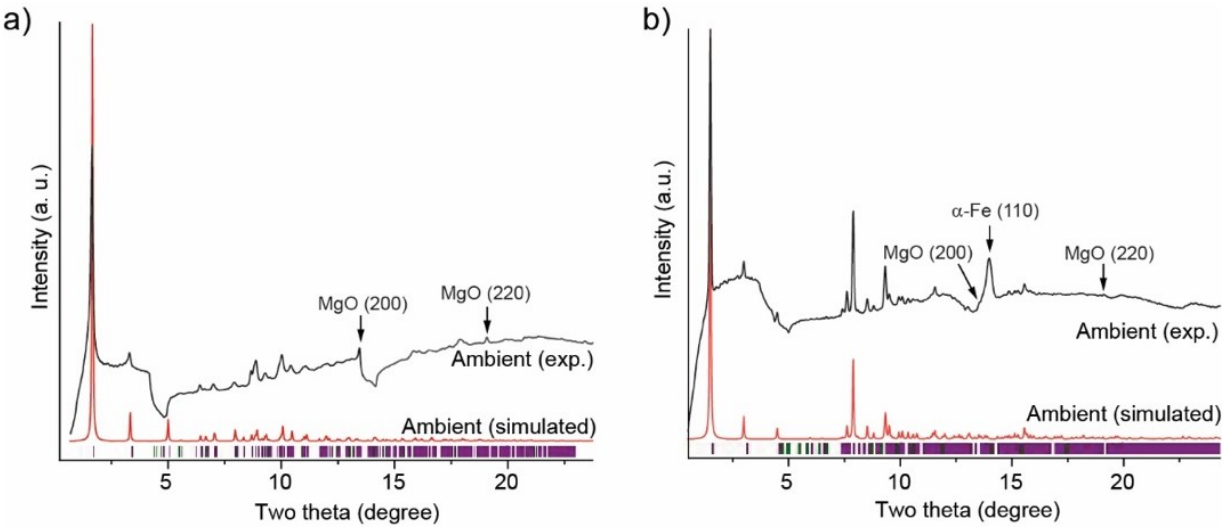

Figure S12. Comparison between experimental (measured in DAC) and simulated XRD pattern at ambient pressure. (a) Co(OH)(sorb). (b) $Mn(sorb)_2$. Wavelength: 0.496 Å. The ticks at the bottom mark the expected positions of the diffraction peaks. The MgO peaks in both samples are used as pressure calibrant. In $Mn(sorb)_2$, the (110) peak of α-Fe (ferrite) is also present, which originates from the stainless steel gasket.

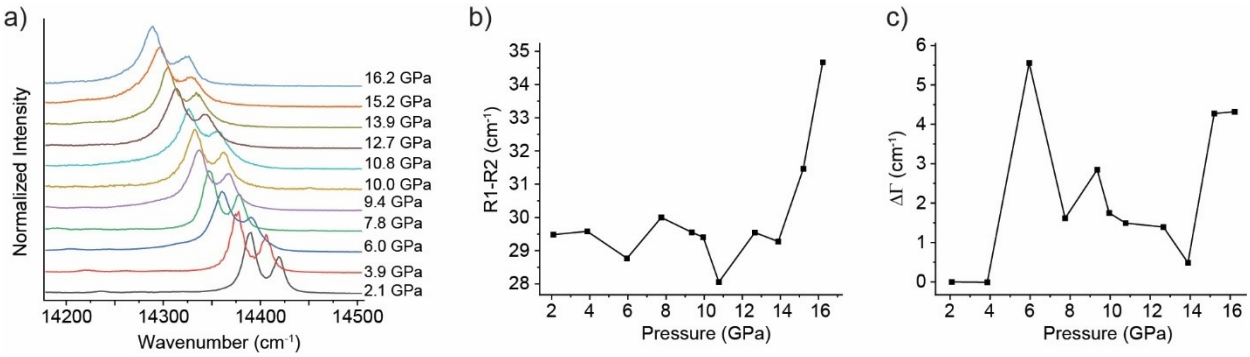

Figure S13. Ruby fluorescence in silicone oil. (a) Fluorescence of ruby at variable pressures. (b) R1-R2 splitting versus pressure. (c) Change of R1 full width at half maximum (ΔΓ) versus pressure.

References

(1) Lefton, J. B.; Liu, W.; McGuire, C.; Lv, B.; Brown, C. M.; Klein, R. A.; Runčevski, T. Synthesis, Structure and Canted Antiferromagnetism of Layered Cobalt Hydroxide Sorbate. *J. Phys. Chem. Solids* **2023**, *182*, 111568. https://doi.org/10.1016/j.jpcs.2023.111568.

(2) Farla, R.; Bhat, S.; Sonntag, S.; Chanyshev, A.; Ma, S.; Ishii, T.; Liu, Z.; Néri, A.; Nishiyama, N.; Faria, G. A.; Wroblewski, T.; Schulte-Schrepping, H.; Drube, W.; Seeck, O.; Katsura, T. Extreme Conditions Research Using the Large-Volume Press at the P61B Endstation, PETRA III. *J. Synchrotron Radiat.* **2022**, *29* (2), 409–423. https://doi.org/10.1107/S1600577522001047.

(3) Klotz, S.; Chervin, J.-C.; Munsch, P.; Le Marchand, G. Hydrostatic Limits of 11 Pressure Transmitting Media. *J. Phys. Appl. Phys.* **2009**, *42* (7), 075413. https://doi.org/10.1088/0022-3727/42/7/075413.

(4) Dorogokupets, P. I.; Oganov, A. R. Ruby, Metals, and MgO as Alternative Pressure Scales: A Semiempirical Description of Shock-Wave, Ultrasonic, x-Ray, and Thermochemical Data at High Temperatures and Pressures. *Phys. Rev. B* **2007**, *75* (2), 024115. https://doi.org/10.1103/PhysRevB.75.024115.

(5) VanNatta, P. E.; Archambault, C. M.; Wang, S.; Lyu, T.; D'Amelio, J.; Martell, N. J.; Watson, S. K.; Wang, K.; Liu, Z.; Kieber-Emmons, M. T.; Yan, H. High Pressure–Derived Nonsymmetrical $[Cu_2\ O]^{2+}$ Core for Room-Temperature Methane Hydroxylation. *Sci. Adv.* **2024**, *10* (40), eadq3366. https://doi.org/10.1126/sciadv.adq3366.

(6) Prescher, C.; Prakapenka, V. B. *DIOPTAS* : A Program for Reduction of Two-Dimensional X-Ray Diffraction Data and Data Exploration. *High Press. Res.* **2015**, *35* (3), 223–230. https://doi.org/10.1080/08957959.2015.1059835.

(7) Prandini, G.; Marrazzo, A.; Castelli, I. E.; Mounet, N.; Marzari, N. Precision and Efficiency in Solid-State Pseudopotential Calculations. *Npj Comput. Mater.* **2018**, *4* (1), 72. https://doi.org/10.1038/s41524-018-0127-2.

(8) Kashinski, D. O.; Chase, G. M.; Nelson, R. G.; Di Nallo, O. E.; Scales, A. N.; VanderLey, D. L.; Byrd, E. F. C. Harmonic Vibrational Frequencies: Approximate Global Scaling Factors for TPSS, M06, and M11 Functional Families Using Several Common Basis Sets. *J. Phys. Chem. A* **2017**, *121* (11), 2265–2273. https://doi.org/10.1021/acs.jpca.6b12147.

(9) Coelho, A. A. Indexing of Powder Diffraction Patterns by Iterative Use of Singular Value Decomposition. *J. Appl. Crystallogr.* **2003**, *36* (1), 86–95. https://doi.org/10.1107/S0021889802019878.

(10) Rietveld, H. M. A Profile Refinement Method for Nuclear and Magnetic Structures. *J. Appl. Crystallogr.* **1969**, *2* (2), 65–71. https://doi.org/10.1107/S0021889869006558.
(11) Pawley, G. S. Unit-Cell Refinement from Powder Diffraction Scans. *J. Appl. Crystallogr.* **1981**, *14* (6), 357–361. https://doi.org/10.1107/S0021889881009618.
(12) Cheary, R. W.; Coelho, A. A.; Cline, J. P. Fundamental Parameters Line Profile Fitting in Laboratory Diffractometers. *J. Res. Natl. Inst. Stand. Technol.* **2004**, *109* (1), 1. https://doi.org/10.6028/jres.109.002.
(13) Andreev, Y. G.; MacGlashan, G. S.; Bruce, P. G. Ab Initio Solution of a Complex Crystal Structure from Powder-Diffraction Data Using Simulated-Annealing Method and a High Degree of Molecular Flexibility. *Phys. Rev. B* **1997**, *55* (18), 12011–12017. https://doi.org/10.1103/PhysRevB.55.12011.
(14) Dinnebier, R. E. Rigid Bodies in Powder Diffraction. A Practical Guide. *Powder Diffr.* **1999**, *14* (2), 84–92. https://doi.org/10.1017/S0885715600010356.